Predictive Force-Centric Emergency Collision Avoidance

Victor Fors[*†]
Division of Vehicular Systems
Department of Electrical Engineering
Linköping University
Linköping, SE-581 83
Sweden
Email: victor.fors@liu.se

Pavel Anistratov[*]
Division of Vehicular Systems
Department of Electrical Engineering
Linköping University
Linköping, SE-581 83
Sweden
Email: pavel.anistratov@liu.se

Björn Olofsson[‡]
Division of Vehicular Systems
Department of Electrical Engineering
Linköping University
Linköping, SE-581 83
Sweden
Email: bjorn.olofsson@liu.se

Lars Nielsen
Division of Vehicular Systems
Department of Electrical Engineering
Linköping University
Linköping, SE-581 83
Sweden
Email: lars.nielsen@liu.se

A controller for critical vehicle maneuvering is proposed that avoids obstacles and keeps the vehicle on the road while achieving heavy braking. It operates at the limit of friction and is structured in two main steps: a motion-planning step based on receding-horizon planning to obtain acceleration-vector references, and a low-level controller for following these acceleration references and transforming them into actuator commands. The controller is evaluated in a number of challenging scenarios and results in a well behaved vehicle with respect to, e.g., the steering angle, the body slip, and the path. It is also demonstrated that the controller successfully balances braking and avoidance, such that it really takes advantage of the braking possibilities. Specifically, for a moving obstacle it makes use of a widening gap to perform more braking, which is a clear advantage of the online replanning capability if the obstacle should be a moving human or animal. Finally, real-time capabilities are demonstrated. In conclusion, the controller performs well, both from a functional perspective and from a real-time perspective.

1 Introduction

The development of automotive sensor systems and automotive situation-awareness systems opens up for new autonomous safety systems. The information about the road borders, surrounding traffic, and possible obstacles on the road can be utilized when devising obstacle-avoidance maneuvers. Using such maneuvers in new safety systems can prevent otherwise fatal or severe crash injuries [1]. They are also central in the context of automated driving, since they can relieve the common requirement of assisted driving systems that the driver should be alert and ready to take over as soon as a critical situation occurs [2]. This is a very hard requirement on a human to switch from a relaxed normal driving situation in a self-driving car to suddenly be alert, and to react quickly and correctly. It is therefore natural that there is significant interest in autonomous safety maneuvers.

There are different options to obtain avoidance strategies [3–5], and one candidate is using optimization [6–9]. In such an optimization formulation, it is natural to use the information from the situation-awareness system, e.g., road borders and obstacles, as constraints in the optimization. Depending on the situation, more or less of the available steering and braking must be used to fulfill the constraints, i.e., to avoid the obstacles while still staying on the road. The remaining actuation freedom can be used for other objectives such as comfort, energy efficiency, or keeping distance to the road boundaries. In an optimization formulation, this objective is specified as an optimization criterion. In previous literature different criteria have been used [3, 6, 8], but in this paper the basic idea is to formulate a criterion that rewards

[*]These authors contributed equally to the work.
[†]Address all correspondence to this author.
[‡]This author is also affiliated with the Department of Automatic Control, Lund University, Lund, SE-221 00, Sweden.

hard braking since lowering the velocity reduces the risk of an accident being severe [10] and could be advantageous when reacting to an obstacle that can move, e.g., a human or an animal (such as a moose). The criterion used is a penalty on velocity v, formulated as an integral of v^2 over a horizon, such that minimizing this integral rewards slowing down the vehicle by hard braking.

Information about if an object is likely to move could be obtained from the situation-awareness system where infrared light can indicate a living object, and if the object is moving, the system can also give estimates of both its speed and direction of motion. An object can block the whole road width, but if it moves a gap could occur behind it. For this reason it is advantageous to adjust and replan as the situation evolves. This can be done using model predictive control, where an optimization is repeated with a shifting finite horizon [11–13]. These repeated optimizations give optimal solutions both in terms of applied control commands and resulting trajectories of state variables. A typical approach then is to use the state trajectories as reference values for a low-level controller giving the actuator commands, see, e.g., [14]. In this paper, a force-based perspective [15–17] is instead used for the low-level controller. Thus, the desired global force (acceleration) on the vehicle from the receding-horizon planning step is used as a reference, and it is, so to say, cascaded down to the wheels in a number of refinement steps. The overall result is force vectoring on the wheels that results in the desired global force and yaw moment on the vehicle.

1.1 Contributions and Outline

A key contribution in this paper is an investigation of the idea of maximum braking while still leaving room for an avoidance maneuver. Further main contributions are the methodology to handle critical situations where a stationary or moving object crosses the road, and the realization of this using a combination of a replanning approach based on receding-horizon control and a force-based low-level controller. This methodology together with selected models enable real-time control while taking advantage of the available tire forces from front-axle steering and individual four-wheel braking.

Section 2 gives a brief background to motion planning as a basis for the overview of the proposed controller that then follows. Continuing with more details of the proposed controller, Section 3 presents the motion-planning step leading to acceleration-vector references, and then Section 4 presents how these acceleration references are turned into actuator commands. The traffic scenarios used are presented in Section 5, and the dynamic vehicle model used for evaluation is presented in Section 6. Section 7 gives the results, whereas discussion and conclusions are given in Sections 8 and 9, respectively.

2 Real-Time Motion Planning

There are two common approaches to motion planning and control in complex scenarios. One approach is to first plan a path around the obstacles and then to follow this path using a path-following controller (see, e.g., [18]). Another common approach is to not only plan a path but also a trajectory. Typically, the trajectory is either directly providing lower-level inputs, such as the steering-wheel angle and the braking forces (see, e.g., [5]), or it can be mapped to such inputs by a low-level controller.

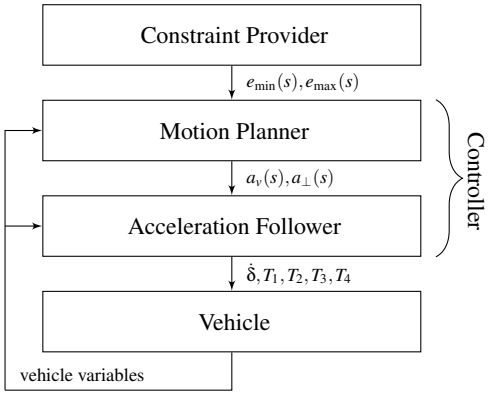

Fig. 1. Control layout

If the scenario is simple enough, it could be possible to obtain an analytical solution of the trajectory [19, 20], but this is not the case for the scenarios considered here. A numerical receding-horizon approach is therefore used to plan the trajectory. The trajectory is planned using a friction-limited particle model giving the desired motion of the center of mass. The controller from [17] is adapted to follow the computed acceleration profile and thus, implicitly, also the resulting path and velocity profile. This approach is in between the aforementioned approaches of motion planning combined with following and directly solving for the control inputs. An overview of the proposed controller is given in the following section.

2.1 Controller Overview

The car considered is capable of front-wheel steering and individual four-wheel braking. The structure of the controller is shown in Fig. 1. A situation-awareness system, which includes a constraint provider, is assumed available. Based on the road borders and obstacles ahead, the constraint provider outputs limits on the drivable area. The controller consists of a real-time motion planner, and an acceleration follower that translates the desired acceleration into steering and braking commands.

At the top level of the controller, a plan is computed that results in a trade-off between using the available forces to reduce the velocity, so as to reduce the severity in case of collision, and using the available forces to avoid collision. The replanning is performed in a receding-horizon fashion, where a friction-limited particle model is used to predict the future movement. Using a friction-limited particle model results in a computationally simpler optimization problem than solving for a full vehicle model. However, the used formulation still captures the difference in friction in the longitudinal and lateral directions. More details on planning are provided in

Section 3.

Aiming to use all available tire forces despite the simple model used for planning, it is assumed that the acceleration reference computed is at the limit of the available tire–road forces. This gives an equivalence between the desired center-of-mass acceleration $[a_v, a_\perp]^{\mathrm{T}}$ and the maximum of a Hamiltonian function [16] (see Section 4.1 for further details)

$$H = p_x F_x + p_y F_y, \tag{1}$$

where F_x is the longitudinal vehicle force, F_y is the lateral vehicle force, and p_x and p_y are values computed from $[a_v, a_\perp]^{\mathrm{T}}$. Because a vehicle is not a particle, the yaw moment M_z is added with a term λ that acts as a Lagrange multiplier, driving the yaw moment to its desired value:

$$H = p_x F_x + p_y F_y + \lambda M_z. \tag{2}$$

Like in the Modified Hamiltonian Algorithm (MHA) [16], this parameter is adapted online such that M_z converges to a desired value M_z^{des}. The vehicle inputs and desired yaw moment M_z^{des} are then determined such that the function H is maximized. This is achieved by the procedure in [17]. First, (1) is maximized to derive an expression for the optimal slip angle of the rear axle α_r^*, around which a control law is formulated to determine M_z^{des}. Then, (2) is maximized to derive expressions for the optimal front-axle slip angles α_1^* and α_2^*, and the optimal braking forces $F_{x,1}^*$, $F_{x,2}^*$, $F_{x,3}^*$, and $F_{x,4}^*$. From these references, control laws are formulated to determine the steering rate $\dot{\delta}$ and wheel braking torques T_1, T_2, T_3, and T_4. A detailed description of the procedure is covered in Section 4.

3 Acceleration References

The acceleration-vector reference is obtained using the particle model described in Section 3.1 in the receding-horizon formulation described in Section 3.2. The particle model is transformed to road-aligned coordinates with path position instead of time as the independent variable. This has the benefits of making it easier to formulate the road boundaries, having one state variable less, and also allowing a fixed-distance planning horizon.

3.1 Particle Model

The motion planner considers the vehicle as a particle controlled by acceleration. With time as the independent variable, the particle motion in global coordinates is described by

$$\dot{X} = v\cos(\xi), \tag{3a}$$
$$\dot{Y} = v\sin(\xi), \tag{3b}$$
$$\dot{v} = a_v - K_d v^2, \tag{3c}$$
$$\dot{\xi} = \frac{a_\perp}{v^2}, \tag{3d}$$

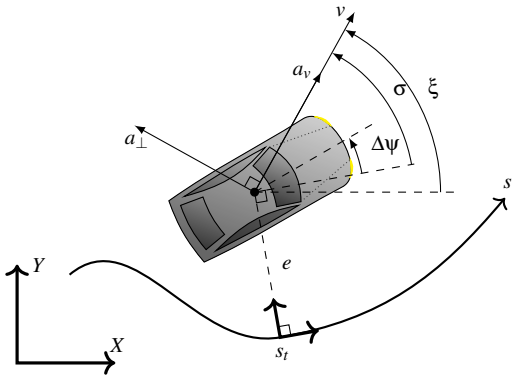

Fig. 2. Vehicle position and orientation in the global coordinates XY and in the road-aligned coordinates at the position $s = s_t$ of the specified path.

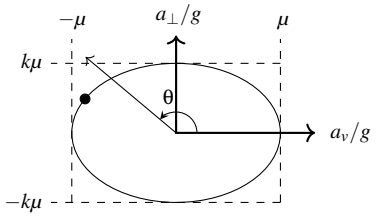

Fig. 3. Illustration of the friction-ellipse limit. The small filled circle denotes the maximum force in the direction indicated by θ.

where X and Y define the global position, v is the magnitude of the velocity vector, and ξ is the orientation of the velocity vector in the global XY-frame. The acceleration is represented by its components a_v and $a_\perp$, where a_v is aligned with the velocity vector (see Fig. 2). The velocity change under influence of drag is modeled by $-K_d v^2$, where K_d is the aerodynamic coefficient. In this vehicle model, the accelerations a_v and $a_\perp$ are the control signals. To model the limited total vehicle forces between the tires and the road, these accelerations are limited by the friction-ellipse [21] relation

$$a_v^2 + (k a_\perp)^2 \leq (\mu g)^2, \tag{4}$$

where k is the ellipse parameter illustrated in Fig. 3, which models the difference in longitudinal and lateral friction potential.

To formulate the road boundaries, the vehicle position is described in road-aligned coordinates [9]. The road is described by a path in the XY-frame, which is the nominal position along the road. Each position s along the path corresponds to a position and orientation in the global XY-frame $[X(s), Y(s), \psi(s)]^{\mathrm{T}}$, which for an initial position s_s along the

path is defined by

$$X(s) = X(s_s) + \int_{s_s}^{s} \cos(\psi)\,\mathrm{d}s, \tag{5a}$$

$$Y(s) = Y(s_s) + \int_{s_s}^{s} \sin(\psi)\,\mathrm{d}s, \tag{5b}$$

$$\psi(s) = \psi(s_s) + \int_{s_s}^{s} \kappa(s)\,\mathrm{d}s, \tag{5c}$$

where $\kappa(s)$ is the path curvature. By taking into account that the lateral velocity, i.e., the velocity perpendicular to the direction defined by σ in Fig. 2, is zero, the state can in the road-aligned frame be described by: the position s along the path, the distance e to the path, the magnitude of the velocity v, and the angle σ to the velocity vector. In these variables, the particle model (3) has the state dynamics [9]

$$\dot{s} = \frac{v\cos(\sigma)}{1-\kappa(s)e}, \tag{6a}$$

$$\dot{e} = v\sin(\sigma), \tag{6b}$$

$$\dot{v} = a_v - K_d v^2, \tag{6c}$$

$$\dot{\sigma} = \dot{\xi} - \kappa(s)\dot{s}. \tag{6d}$$

By considering s as an independent variable and using (6a), the element $\mathrm{d}t$ is expressed as

$$\mathrm{d}t = \frac{\mathrm{d}t}{\mathrm{d}s}\mathrm{d}s = \frac{1-\kappa(s)e}{v\cos(\sigma)}\mathrm{d}s. \tag{7}$$

Using (6) and (7), and defining the state vector $\mathbf{x} = [e, \sigma, v^2]^{\mathrm{T}}$ and the input vector $\mathbf{u} = [a_v, a_\perp]^{\mathrm{T}}$, the motion of a particle in the global coordinates (3) is now expressed in the path coordinates as

$$\mathbf{x}' = \frac{\mathrm{d}\mathbf{x}}{\mathrm{d}s} = G(\mathbf{x},\mathbf{u}) = \begin{bmatrix} \frac{\mathrm{d}e}{\mathrm{d}t}\frac{\mathrm{d}t}{\mathrm{d}s} \\ \frac{\mathrm{d}\sigma}{\mathrm{d}t}\frac{\mathrm{d}t}{\mathrm{d}s} \\ 2v\frac{\mathrm{d}v}{\mathrm{d}t}\frac{\mathrm{d}t}{\mathrm{d}s} \end{bmatrix} = \begin{bmatrix} (1-\kappa(s)e)\tan(\sigma) \\ \frac{(1-\kappa(s)e)a_\perp}{v^2\cos(\sigma)} - \kappa(s) \\ \frac{2(1-\kappa(s)e)(a_v - K_d v^2)}{\cos(\sigma)} \end{bmatrix}. \tag{8}$$

3.2 Receding-Horizon Planning

For a specified planning cycle defined in distance s, the motion planner provides the input vector $\mathbf{u}$ by solving an optimal control problem. The problem is to minimize the integral of the squared velocity between positions s_s and s_f for the particle (represented by the dynamic constraints (8)) starting at the state $\mathbf{x}_s$ and staying within the limits of the drivable area, $e_{\min}(s)$ and $e_{\max}(s)$, defined by the constraint provider (see Fig. 1):

$$\underset{\mathbf{x},\mathbf{u}}{\text{minimize}} \quad \int_{s_s}^{s_f} v^2\,\mathrm{d}s \tag{9a}$$

$$\text{subject to} \quad \mathbf{x}(s_s) = \mathbf{x}_s,\ \mathbf{x}' = G(\mathbf{x},\mathbf{u}), \tag{9b}$$

$$e_{\min}(s) \le e(s) \le e_{\max}(s), \tag{9c}$$

$$a_v^2 + (ka_\perp)^2 \le (\mu g)^2,\ a_v \le 0, \tag{9d}$$

where the acceleration inputs a_v and $a_\perp$ are constrained by the friction-ellipse (4) and are limited to braking of the vehicle.

The continuous optimal control problem (9) is discretized using the forward Euler method for $N+1$ discrete points with the step size Δs and the variables are indexed by $i \in \{0,\ldots,N\}$. The discretized dynamics with piecewise constant control inputs is included in the resulting numerical optimization using the multiple shooting method [22]. For improved handling of the road-boundary conditions, taking into account uncertainties in the model, functions penalizing driving closer than the distance e_{margin} to the boundaries are formulated for the left and right road boundary as

$$p_{\text{left},i} = \max(e_i - e_{\max,i} + e_{\text{margin}}, 0), \tag{10a}$$

$$p_{\text{right},i} = \max(e_{\min,i} - e_i + e_{\text{margin}}, 0). \tag{10b}$$

Finally, a possible small change in the friction coefficient μ is introduced as a slack variable like in [11]. The coefficient μ is typically set using a conservative estimate smaller than the actual value. When it is required to find a feasible solution, the solver is allowed to increase μ relative to its conservative estimate $\hat{\mu}$. The increase in the friction coefficient μ comes at the cost of a penalty on their difference

$$(\mu - \hat{\mu})^2, \tag{11}$$

and the corresponding weighting factor c_μ in the criterion (12a) is set very high as in [11]. Then, after the problem has been solved, the resulting μ is checked for an indication if the resulting trajectory is possible to follow by the vehicle. As long as the resulting μ is below the actual effective friction coefficient of the vehicle, it is possible that the vehicle can avoid collision. Finally, the resulting optimization problem based on (9) that is solved numerically is

$$\underset{\mathbf{x},\mathbf{u},\mu}{\text{minimize}} \quad \sum_{i=0}^{N} \left(v_i^2 + c_e p_{\text{left},i}^2 + c_e p_{\text{right},i}^2 + c_\mu(\mu-\hat{\mu})^2\right) \tag{12a}$$

$$\text{subject to} \quad \mathbf{x}_0 = \mathbf{x}_s,\ \mathbf{x}_{i+1} = \mathbf{x}_i + \Delta s G(\mathbf{x}_i,\mathbf{u}_i), \tag{12b}$$

$$e_{\min,i} \le e_i \le e_{\max,i}, \tag{12c}$$

$$a_{v,i} \le \sqrt{(\mu g)^2 - (ka_{\perp,i})^2}, \tag{12d}$$

$$a_{v,i} \ge -\sqrt{(\mu g)^2 - (ka_{\perp,i})^2}, \tag{12e}$$

$$-\mu g \le a_{v,i} \le 0,\ -\mu g \le ka_{\perp,i} \le \mu g, \tag{12f}$$

$$v_i^2 \ge v_{\min}^2,\ \sigma_{\min} \le \sigma_i \le \sigma_{\max}, \tag{12g}$$

where c_e and c_μ are weighting factors for the penalties (10) and (11). However, the main focus of the objective function (12a) is still to decrease the velocity, since the weighting factors are chosen such that the additional penalties nominally have small values and they are only included to improve real-time performance. For computational performance, the constraints (9d) are reformulated to the constraints (12d) – (12f), where the constraints (12f) do not put new restrictions

on the acceleration vector with respect to (9d) as it is just a bounding box (see the dashed lines in Fig. 3). The constraints (12g) are added to avoid the state values for which the model (8) is undefined, where $v^2_{\min}$, $\sigma_{\min}$, and $\sigma_{\max}$ are user-defined parameters.

The resulting nonlinear optimization problem (12) is solved using CasADi [23], IPOPT [24], and HSL MA57 [25]. To reduce the computation time of the motion planner, CasADi is used to create a parametric function that solves the problem (12), where the parameters specify initialization values of the variables, the current vehicle state, and the obstacle configuration. The parametric function is created using automatic differentiation to generate expressions for numerical evaluation [23]. This is done only once, ahead of time, which reduces the overhead as opposed to declaring the problem at each iteration. The computational performance of the motion planner is demonstrated in Section 7.4.

The time to drive the planning-cycle distance is allocated for the motion planner to compute a plan for the next starting position s_s. The state $\mathbf{x}_s$ is predicted by integrating the model (8) using the current state of the vehicle and the input $\mathbf{u}$ from the previous plan. When the problem (12) is solved for the first time, the future state is obtained under the assumption of maximum straight-line braking. The velocities, $v_i^2 \ \forall \ i \in \{0,\dots,N\}$, are initialized to the velocity v_s^2 to avoid initial division by zero in the model (8). The lateral distances to the path, $e_i \ \forall \ i \in \{0,\dots,N\}$, are initialized to the center line between the path boundaries (39)

$$e_{i,\text{init}} = \frac{e_{\min}(s_i) + e_{\max}(s_i)}{2}. \tag{13}$$

The other states are initialized to zero. The Lagrange multipliers of the constraints (12b)–(12g) are reused from the previous plan for initialization at the next optimization.

4 Acceleration Following

The goal is to follow the acceleration-vector reference computed by the motion planner in Section 3 via control of the steering-wheel rate $\dot{\delta}$ and wheel braking torques $T_i,\ i \in \{1,2,3,4\}$. This is achieved by applying the control structure from [17]. Compared to that paper, the controller is here tailored to better follow acceleration-vector references computed by the motion planner in Section 3.

4.1 Center-of-Mass Acceleration Reference

It is assumed that the desired acceleration $[a_v, a_\perp]^\text{T}$ obtained from the motion planner is at the limit of the tire–road friction. Then, as illustrated in Fig. 3, there is an equivalence between the desired acceleration and the acceleration defined by the angle θ. The variable φ is introduced to represent the desired acceleration at the friction-ellipse limit:

$$a_v = \mu g \cos(\varphi), \tag{14a}$$
$$a_\perp = \frac{\mu g}{k} \sin(\varphi). \tag{14b}$$

This relation can also be written as

$$\frac{k a_\perp}{a_v} = \tan(\varphi). \tag{15}$$

Using (14), an equivalent of the Hamiltonian (1) in terms of acceleration components is

$$\begin{aligned} H &= a_v \cos(\theta) + a_\perp \sin(\theta) \\ &= \mu g \cos(\varphi)\cos(\theta) + \frac{\mu g}{k} \sin(\varphi)\sin(\theta). \end{aligned} \tag{16}$$

To maximize this function with respect to φ, its derivative is examined

$$\frac{\mathrm{d}H}{\mathrm{d}\varphi} = -\mu g \sin(\varphi)\cos(\theta) + \frac{\mu g}{k} \cos(\varphi)\sin(\theta), \tag{17}$$

which is zero when

$$\tan(\theta) = k \tan(\varphi) = \frac{k^2 a_\perp}{a_v}. \tag{18}$$

Because there are clearly two extrema, one on each side of the ellipse, it is also ensured that the second-order derivative is negative, i.e.,

$$\begin{aligned} \frac{\mathrm{d}^2 H}{\mathrm{d}\varphi^2} &= -\mu g \cos(\varphi)\cos(\theta) - \frac{\mu g}{k} \sin(\varphi)\sin(\theta) \\ &= -H < 0. \end{aligned} \tag{19}$$

The angle θ, i.e., the direction relative to the velocity vector in which maximizing the acceleration (force) gives the desired acceleration, is then computed by

$$\theta = \operatorname{arctan2}(k^2 a_\perp, a_v). \tag{20}$$

Before using this angle, it is transformed into the road-aligned coordinates using the planned direction of the velocity vector σ,

$$\theta^s = \operatorname{arctan2}(k^2 a_\perp(s), a_v(s)) + \sigma(s). \tag{21}$$

It is then transformed into the vehicle coordinates by the measured value of the vehicle orientation $\Delta\psi$ (see Fig. 2) at the current time t,

$$\theta^v = \theta^s(s) - \Delta\psi(t). \tag{22}$$

Finally, the values of p_x and p_y in the Hamiltonian (1) are computed as

$$p_x = \cos(\theta^v), \tag{23a}$$
$$p_y = \sin(\theta^v). \tag{23b}$$

4.2 Wheel-Level Force References

The sum of the forces from all wheels results in the total yaw moment M_z acting on the vehicle. To control this yaw moment, the procedure from [16] is used, where λ in the modified Hamiltonian (2) is adapted online to achieve the desired yaw moment M_z^{des}. This is done with the following update at each controller sampling instant, using the same formula as in [26]:

$$\lambda \to \lambda + S\tanh(\varepsilon(M_z^{\text{des}} - M_z)), \tag{24}$$

where S and ε are parameters determining the size of the change in λ. To prevent λ from getting too large if M_z^{des} cannot quickly be achieved, λ is saturated at $\pm\lambda_{\max}$. To approximate the yaw moment M_z in the update (24), the friction-ellipse model with combined slip and the simplified Pacejka's Magic Formula [21] is used to compute the lateral tire force $F_{y,i}$ where the longitudinal tire force is obtained from the applied braking torque T_i:

$$F_{y0,i} = \mu_{y,i} F_{z,i} \sin(C_{y,i} \arctan(B_{y,i}\alpha_i)), \tag{25a}$$
$$F_{x,i} = T_i R_e, \tag{25b}$$
$$F_{y,i} = F_{y0,i}\sqrt{1 - \frac{F_{x,i}}{\mu_{x,i} F_{z,i}}}, \tag{25c}$$

where $F_{z,i}$ is the vertical load, α_i is the slip angle computed taking the relaxation length into account (42), R_e is the effective wheel radius, $B_{y,i}$, $C_{y,i}$, $\mu_{x,i}$, and $\mu_{y,i}$ are tire parameters (Table 2), and the rotational wheel dynamics is assumed to be in steady state. The forces F_x and F_y and the yaw moment M_z acting on the vehicle are the sums of the individual tire forces

$$F_{x,i}^v = F_{x,i}\cos(\delta_i) - F_{y,i}\sin(\delta_i), \tag{26a}$$
$$F_{y,i}^v = F_{x,i}\sin(\delta_i) + F_{y,i}\cos(\delta_i), \tag{26b}$$
$$F_x = \sum_{i=1}^{4} F_{x,i}^v, \tag{26c}$$
$$F_y = \sum_{i=1}^{4} F_{y,i}^v, \tag{26d}$$
$$M_z = \sum_{i=1}^{4} (l_{x,i} F_{y,i}^v - l_{y,i} F_{x,i}^v), \tag{26e}$$

where $l_{x,i}$ and $l_{y,i}$ are the longitudinal and lateral distances from the center of mass, respectively.

Assuming that the actuators acting on each wheel are independent of each other, the functions (1) and (2) are reduced and solved independently for each wheel. To maximize the Hamiltonian (1), the direction $[p_{x,i}, p_{y,i}]^{\mathrm{T}}$ expressed in local wheel coordinates to maximize the force in is

$$p_{x,i} = \cos(\theta^v - \delta_i), \tag{27a}$$
$$p_{y,i} = \sin(\theta^v - \delta_i), \tag{27b}$$

where δ_i is the steering angle of the ith wheel. Considering the modified Hamiltonian (2), where yaw moment is controlled, the direction $[\tilde{p}_{x,i}, \tilde{p}_{y,i}]^{\mathrm{T}}$ in local wheel coordinates that maximizes the Hamiltonian (2) is, by substituting F_x, F_y, and M_z using (26), given by

$$\tilde{\theta}^v = \arctan2(\sin(\theta^v) + \lambda l_{x,i}, \cos(\theta^v) - \lambda l_{y,i}), \tag{28a}$$
$$\tilde{p}_{x,i} = \cos(\tilde{\theta}^v - \delta_i), \tag{28b}$$
$$\tilde{p}_{y,i} = \sin(\tilde{\theta}^v - \delta_i). \tag{28c}$$

4.3 Desired Slip Angles

To compute the desired slip angles, the desired lateral tire forces are determined. The slip angles of the rear wheels are determined by the vehicle motion, while the slip angles of the front wheels are controlled by a common front-axle steering angle. As reference for the yaw control (Section 4.4), the lumped rear slip angle α_r of the rear axle is used, while for the steering control (Section 4.5), the individual slip angles of the front wheels, α_1 and α_2, are considered. How these possibly conflicting slip angles are handled is explained in Section 4.5.

Similar to how the target acceleration-vector reference $[p_x, p_y]^{\mathrm{T}}$ is computed in Section 4.1 based on the friction ellipse representing the acceleration potential of the whole vehicle, the desired lateral tire force $F_{y,i}^*$ is computed on the friction ellipse resulting from tire–road forces:

$$F_{z,i}^2 = \left(\frac{F_{x,i}^*}{\mu_{x,i}}\right)^2 + \left(\frac{F_{y,i}^*}{\mu_{y,i}}\right)^2, \tag{29}$$

where $F_{x,i}^*$ is the corresponding optimal braking force. Because the purpose of controlling the yaw moment is to control the rear slip angles, the rear slip angles are not used to control the yaw moment. The desired lateral force $F_{y,r}^*$ maximizes the force of the rear tires in the direction $[p_x, p_y]^{\mathrm{T}}$ and is computed as [17]

$$F_{y,r}^* = F_{z,r}\mu_{y,r}\sin(\arctan2(\mu_{y,r}p_{y,r}, \mu_{x,r}p_{x,r})). \tag{30}$$

To avoid generating unexpected lateral tire forces, when correcting the yaw moment, but still reducing the lateral tire force if necessary (to not overly saturate the tire forces if differential braking is desired), the desired lateral forces $F_{y,1}^*$ and $F_{y,2}^*$ of the front tires are computed as

$$\begin{bmatrix}\hat{p}_{x,i}\\ \hat{p}_{y,i}\end{bmatrix} = \begin{cases}\begin{bmatrix}\tilde{p}_{x,i}\\ \tilde{p}_{y,i}\end{bmatrix} & \text{if } |\tilde{p}_{y,i}| < |p_{y,i}|,\\ \begin{bmatrix}p_{x,i}\\ p_{y,i}\end{bmatrix} & \text{otherwise,}\end{cases} \tag{31a}$$
$$F_{y,i}^* = F_{z,i}\mu_{y,i}\sin(\arctan2(\mu_{y,i}\hat{p}_{y,i}, \mu_{x,i}\hat{p}_{x,i})). \tag{31b}$$

To find the desired slip angle from the desired lateral tire force, a tire model on the form of a simplified Pacejka's

Magic Formula [21] is used. Rather than specifying the model at zero longitudinal tire force as is commonly done, it is as in [17] specified at the friction-ellipse boundary (29):

$$F^*_{y,i}(\alpha_i) = F_{z,i}\mu_{y,i}\sin(C^*_{y,i}\arctan(B^*_{y,i}\alpha_i)), \tag{32}$$

where $B^*_{y,i}$ and $C^*_{y,i}$ are tire parameters. Here, the function (32) is precomputed from the complete model of the longitudinal and lateral tire forces described in Section 6 as function of the steady-state values for the tire slips. The tire model (32) is inverted to compute the desired slip angle

$$\alpha^*_i = \frac{1}{B^*_{y,i}}\tan\left(\frac{1}{C^*_{y,i}}\arcsin\left(\frac{F^*_{y,i}}{F_{z,i}\mu_{y,i}}\right)\right). \tag{33}$$

4.4 Yaw Control

A control law is formulated like [17] to determine the desired yaw moment M_z^{des} to achieve the desired slip angle α^*_r of the rear axle. To handle chattering due to quick changes in α^*_r caused by replanning, a first-order filter with the time constant τ_r is incorporated. Using small-angle approximations of the body slip β and the slip angle α_r, the control law to achieve α^*_r is obtained from the characteristic equation of a stable second-order system with poles at $-\omega$ as

$$M_z^{\text{des}}/I_{zz} = \dot{r}^{\text{des}} = -2\omega\dot{\beta}^e - \omega^2\beta^e, \tag{34a}$$

$$\beta^e = -\alpha_r^{\text{des}} - \frac{v_y - l_r r}{v_x}, \tag{34b}$$

$$\dot{\beta}^e = -\dot{\alpha}_r^{\text{des}} - \frac{\dot{v}_y}{v_x} + \frac{(v_y - l_r r)\dot{v}_x}{v_x^2}, \tag{34c}$$

$$\tau_r\dot{\alpha}_r^{\text{des}} = \alpha^*_r - \alpha_r^{\text{des}}, \tag{34d}$$

where r is the yaw rate, and l_r is the distance between the rear axle and the vehicle center of mass. It is assumed that the yaw acceleration $\dot{r}$ converges to a small value as β^e and $\dot{\beta}^e$ approach zero, allowing terms with $\dot{r}$ to be discarded. To prevent excessive yaw-moment demands that cannot be fulfilled, M_z^{des} is saturated at $\pm mgw/2$, where w is the half-width of the car.

4.5 Steering Control

To handle chattering due to quick changes in α^*_i caused by replanning, a first-order filter with time constant τ_i is incorporated in the steering controller. The control law is synthesized similar to [27] with the feedback gain K by the stable dynamics

$$\dot{\alpha}_i - \dot{\alpha}_i^{\text{des}} = -K(\alpha_i - \alpha_i^{\text{des}}), \tag{35a}$$

$$\tau_i\dot{\alpha}_i^{\text{des}} = \alpha^*_i - \alpha_i^{\text{des}}. \tag{35b}$$

Disregarding the influence of the yaw acceleration and using a small-angle approximation of the slip angle gives the desired steering rate of wheel i as

$$\dot{\delta}_i^{\text{des}} = K(\alpha_i^{\text{des}} - \alpha_i) + \frac{\dot{v}_y}{v_x - l_{y,i}r} - \frac{\dot{v}_x(v_y + l_{x,i}r)}{(v_x - l_{y,i}r)^2}. \tag{36}$$

Because there is only one steering angle but two desired steering rates (one for each of the two front wheels), the steering rate is determined by

$$\dot{\delta} = \begin{cases} \dot{\delta}_1^{\text{des}} & \text{if } \dot{\delta}_1^{\text{des}}\alpha_{\text{sign}} < \dot{\delta}_2^{\text{des}}\alpha_{\text{sign}}, \\ \dot{\delta}_2^{\text{des}} & \text{otherwise,} \end{cases} \tag{37}$$

where $\alpha_{\text{sign}} = \text{sign}(\alpha_1 + \alpha_2)$. This acts to steer towards reducing the slip angles, enabling differential braking without overly saturating the tires.

4.6 Braking Control

To compute the braking torques, it is assumed that the wheel dynamics is in steady state. The friction-ellipse based model (25) is used, which allows an analytical solution to the problem of maximizing the Hamiltonian (2) with respect to the braking forces (a new ellipse with reduced lateral friction) [17]. With the braking torques acting independently, this corresponds to maximizing the individual tire forces in the direction of $[\tilde{p}_x, \tilde{p}_y]^{\text{T}}$. Because only braking is considered, the braking force is saturated between $-\mu_{x,i}F_{z,i}\cos(\alpha_i)$ and 0, where the lower limit corresponds to a locked wheel with saturated tire forces. To prevent undesired locking of the wheels, slip control could be used. Here for simplicity, this is solved by reducing the braking torques with a scaling factor γ_T. In summary, the torque for each tire is computed with

$$F^*_{x,i} = \mu_{x,i}F_{z,i}\cos\left(\arctan2\left(\frac{F_{y0,i}}{F_{z,i}}\tilde{p}_{y,i}, \mu_{x,i}\tilde{p}_{x,i}\right)\right), \tag{38a}$$

$$F_{x,\min} = -\mu_{x,i}F_{z,i}\cos(\alpha_i), \tag{38b}$$

$$F_{x,\max} = 0, \tag{38c}$$

$$T_i = \begin{cases} \gamma_T R_e F_{x,\max} & \text{if } F^*_{x,i} > F_{x,\max}, \\ \gamma_T R_e F_{x,\min} & \text{if } F^*_{x,i} < F_{x,\min}, \\ \gamma_T R_e F^*_{x,i} & \text{otherwise.} \end{cases} \tag{38d}$$

4.7 Summary of Computations

The computations presented in Sections 4.1–4.6 are summarized as:

1. Compute the desired center-of-mass acceleration-vector reference θ^v (22).
2. Compute the desired tire-force vector references $[p_{x,i}, p_{y,i}]^{\text{T}}$, $i \in \{1,2,r\}$, (27).
3. Compute the desired slip angle α^*_r of the rear axle (30), (33).
4. Determine the desired yaw moment M_z^{des} (34).
5. Estimate the yaw moment M_z (25), (26).
6. Update λ to track M_z^{des} (24).

7. Compute the desired tire-force vector references $[\tilde{p}_{x,i}, \tilde{p}_{y,i}]^{\mathrm{T}}$, $i \in \{1,2,3,4\}$ (28).
8. Compute the desired front-wheel slip angles α_1^* and α_2^* (31), (33).
9. Determine the desired steering rate $\dot{\delta}$ (35b), (36), (37).
10. Compute the desired braking torques T_i, $i \in \{1,2,3,4\}$, (38).

5 Scenarios

A number of scenarios are used to evaluate the performance of the controller. The chosen roads are of different curvature, posing different levels of difficulty to stay on road after the obstacle. Both stationary and moving obstacles are considered, specifically the case when an obstacle moves across the road such that the gap widens after it. The initial speed used is a normal driving speed for the road in consideration, and thus the criticality of the situation comes from the unexpected occurrence of an obstacle.

The investigated scenarios are obstacle avoidance where the vehicle is traveling at 90 km/h. The lateral margin that the vehicle has to maneuver from its nominal center position is ± 2.5 m. A moose is detected on the road 21 m ahead of the vehicle. The moose is facing towards the right relative to the vehicle and it is assumed that the moose can quickly walk forwards, such that the road in front of the moose is effectively blocked, but that it will not quickly turn around or move backwards. When it moves forward, i.e., to the side off the road, it is with the speed v_{obs}. The drivable area defined by the constraint provider (see Fig. 1) is reduced to take the size of the vehicle into consideration. Mathematically, the path boundaries in the scenarios are defined as

$$e_{\min}(s,t) = \begin{cases} 1.3 - v_{\mathrm{obs}} t, & \text{if } 20 \le s \le 22, \\ -2.5, & \text{otherwise,} \end{cases} \tag{39a}$$

$$e_{\max}(s,t) = 2.5, \tag{39b}$$

where the scenarios start at time $t = 0$, and the sizes of the moose and car result in the reduced margin at 20 m to 22 m ahead of the initial vehicle position.

6 Evaluation Model

To evaluate the performance of the controller, it is examined in simulation using a double-track vehicle model with longitudinal and lateral load transfer (see [28]), and wheel dynamics with the tire forces modeled using Pacejka's Magic Formula [21] with weighting functions [21]. The model is the same as the one denoted DT-WF in [8], with the modifications of using the load-transfer equations (55) – (58) and adding wind resistance. The model equations are well known and are here only briefly presented for completeness. The model has the 19 variables described in Table 1 and is on the form of a semi-explicit DAE (differential-algebraic system of equations), where the algebraic variables are resulting from load transfer. The inputs are the steering rate $\dot{\delta}$ and the braking torque to each wheel T_1, T_2, T_3, and T_4.

Table 1. Vehicle variables

Description	Notation
Position and orientation	$s, e, \Delta\psi$
Velocity and yaw rate	v_x, v_y, r
Steering angle	δ
Rotational wheel speeds	$\omega_1, \omega_2, \omega_3, \omega_4$
Wheel slip angles	$\alpha_1, \alpha_2, \alpha_3, \alpha_4$
Vertical tire loads	$F_{z,1}, F_{z,2}, F_{z,3}, F_{z,4}$

The local velocity at each wheel i is given by

$$v_{x,i} = (v_x - r l_{y,i})\cos(\delta_i) + (v_y + r l_{x,i})\sin(\delta_i), \tag{40}$$

$$v_{y,i} = (v_y + r l_{x,i})\cos(\delta_i) - (v_x - r l_{x,i})\sin(\delta_i), \tag{41}$$

where $\delta_1 = \delta_2 = \delta$ and $\delta_3 = \delta_4 = 0$. The equations for the tire slips are [21]

$$\dot{\alpha}_i = \frac{v_{x,i}}{\sigma_{\mathrm{r}}} \left(-\arctan\left(\frac{v_{y,i}}{v_{x,i}}\right) - \alpha_i \right), \tag{42}$$

$$\kappa_i = \frac{R_e \omega_i - v_{x,i}}{v_{x,i}}, \tag{43}$$

where σ_{r} is the relaxation length. The tire model, Pacejka's Magic Formula [21] with weighting functions [21], is:

$$F_{x0,i} = \mu_{x,i} F_{z,i} \sin(C_{x,i} \arctan(B_{x,i}\kappa_i - E_{x,i}(B_{x,i}\kappa_i - \arctan(B_{x,i}\kappa_i)))), \tag{44}$$

$$F_{y0,i} = \mu_{y,i} F_{z,i} \sin(C_{y,i} \arctan(B_{y,i}\alpha_i - E_{y,i}(B_{y,i}\alpha_i - \arctan(B_{y,i}\alpha_i)))), \tag{45}$$

$$G_{x,i} = \cos(C_{x\alpha,i} \arctan(B_{x1,i} \cos(\arctan(B_{x2,i}\kappa_i))\alpha_i)), \tag{46}$$

$$G_{y,i} = \cos(C_{y\kappa,i} \arctan(B_{y1,i} \cos(\arctan(B_{y2,i}\alpha_i))\kappa_i)), \tag{47}$$

$$F_{x,i} = G_{x,i} F_{x0,i}, \tag{48}$$

$$F_{y,i} = G_{y,i} F_{y0,i}, \tag{49}$$

where B, C, and E are tire-dependent parameters. The forces on the chassis are given by

$$F_{x,i}^v = F_{x,i}\cos(\delta_i) - F_{y,i}\sin(\delta_i), \tag{50}$$

$$F_{y,i}^v = F_{x,i}\sin(\delta_i) + F_{y,i}\cos(\delta_i), \tag{51}$$

$$F_x = \sum_{i=1}^{4} \left(F_{x,i}^v - K_D v_x \sqrt{v_x^2 + v_y^2} \right), \tag{52}$$

$$F_y = \sum_{i=1}^{4} \left(F_{y,i}^v - K_D v_y \sqrt{v_x^2 + v_y^2} \right), \tag{53}$$

$$M_z = \sum_{i=1}^{4} (l_{x,i} F_{y,i}^v - l_{y,i} F_{x,i}^v), \tag{54}$$

where K_D is the aerodynamic coefficient. The vertical loads are computed by

$$\sum_{i=1}^{4} F_{z,i} - mg = 0, \tag{55}$$

Table 2. Vehicle parameters. The values are adopted from [8] and [21].

Notation	Value
g	$9.81\,\mathrm{m/s}$
$l_{x,1}$, $l_{x,2}$	$1.3\,\mathrm{m}$
$l_{x,3}$, $l_{x,4}$	$-1.5\,\mathrm{m}$
$l_{y,1}$, $l_{y,3}$	$0.8\,\mathrm{m}$
$l_{y,2}$, $l_{y,4}$	$-0.8\,\mathrm{m}$
w	$0.8\,\mathrm{m}$
h	$0.5\,\mathrm{m}$
m	$2100\,\mathrm{kg}$
I_{zz}	$3900\,\mathrm{kg\,m^2}$
R_e	$0.3\,\mathrm{m}$
I_ω	$2\,\mathrm{kg\,m^2}$
σ_r	$0.3\,\mathrm{m}$
K_D	$0.36\,\mathrm{kg/m}$
$\mu_{x,1}$, $\mu_{x,2}$	1.1959
$B_{x,1}$, $B_{x,2}$	11.6848
$C_{x,1}$, $C_{x,2}$	1.685
$E_{x,1}$, $E_{x,2}$	0.37729
$\mu_{y,1}$, $\mu_{y,2}$	0.93476
$B_{y,1}$, $B_{y,2}$	8.8626
$C_{y,1}$, $C_{y,2}$	1.193
$E_{y,1}$, $E_{y,2}$	−1.2076
$\mu_{x,3}$, $\mu_{x,4}$	1.2027
$B_{x,3}$, $B_{x,4}$	11.1217
$C_{x,3}$, $C_{x,4}$	1.685
$E_{x,3}$, $E_{x,4}$	0.36192
$\mu_{y,3}$, $\mu_{y,4}$	0.96146
$B_{y,3}$, $B_{y,4}$	9.3016
$C_{y,3}$, $C_{y,4}$	1.193
$E_{y,3}$, $E_{y,4}$	−1.1087
$C_{x\alpha,1}$, $C_{x\alpha,2}$, $C_{x\alpha,3}$, $C_{x\alpha,4}$	1.092
$B_{x1,1}$, $B_{x1,2}$, $B_{x1,3}$, $B_{x1,4}$	12.35
$B_{x2,1}$, $B_{x2,2}$, $B_{x2,3}$, $B_{x2,4}$	−10.77
$C_{y\kappa,1}$, $C_{y\kappa,2}$, $C_{y\kappa,3}$, $C_{y\kappa,4}$	1.081
$B_{y1,1}$, $B_{y1,2}$, $B_{y1,3}$, $B_{y1,4}$	6.461
$B_{y2,1}$, $B_{y2,2}$, $B_{y2,3}$, $B_{y2,4}$	4.196

$$\sum_{i=1}^{4} l_{x,i}F_{z,i} + hF_x = 0, \tag{56}$$

$$\sum_{i=1}^{2} l_{y,i}F_{z,i} + \frac{hF_y}{2} = 0, \tag{57}$$

$$\sum_{i=3}^{4} l_{y,i}F_{z,i} + \frac{hF_y}{2} = 0, \tag{58}$$

where h is the height of the center of mass and m is the mass of the vehicle. The wheel dynamics is modeled as

$$\dot{\omega}_i = \frac{T_i - F_{x,i}R_e}{I_\omega}, \tag{59}$$

where I_ω is the wheel inertia, and the chassis dynamics are

$$\dot{v}_y = \frac{F_y}{m} - rv_x, \tag{60}$$

$$\dot{v}_x = \frac{F_x}{m} + rv_y, \tag{61}$$

$$\dot{r} = \frac{M_z}{I_{zz}}. \tag{62}$$

The state dynamics of the road coordinates (see Fig. 2) is obtained from

$$\dot{s} = \frac{v_x\cos(\Delta\psi) - v_y\sin(\Delta\psi)}{1-\kappa(s)e}, \tag{63}$$

$$\dot{e} = v_x\sin(\Delta\psi) + v_y\cos(\Delta\psi), \tag{64}$$

$$\Delta\dot{\psi} = r - \kappa(s)\dot{s}. \tag{65}$$

7 Results

The proposed controller is evaluated in the scenarios described in Section 5 using the vehicle model in Section 6. The scenarios are treated in the following subsections in an order starting with the straight-road scenario, then the curved-road scenarios, and finally the scenario with the moving obstacle. The initial speed is $90\,\mathrm{km/h}$, and the obstacle appears $20\,\mathrm{m}$ ahead as can be seen mathematically in (39) and also in, e.g., Fig. 4.

The low-level controller for acceleration-reference following in Section 4 is explicit in the computations and is executed at $1000\,\mathrm{Hz}$. The motion planner in Section 3 is set to provide a new plan every $2\,\mathrm{m}$ of traveled distance along the road, which corresponds to a new plan every $80\,\mathrm{ms}$ when driving at $90\,\mathrm{km/h}$.

Numerical values of the parameters used in the motion planner are given in Table 3. The planning horizon $s_f - s_s$ of $30\,\mathrm{m}$ is selected some distance longer than the initial distance of $20\,\mathrm{m}$ to the obstacle and is the same for all plans. Increasing the planning horizon further does not improve the quality of the plans in the scenarios examined. The friction coefficient $\hat{\mu}$ is set to 90 % of the lumped longitudinal friction coefficients of the vehicle and the ellipse parameter k is set to the ratio between the lumped longitudinal friction coefficients and the lumped lateral friction coefficients. The parameter c_μ is set to a large value so that a significantly higher friction coefficient is only used if the problem with the friction $\mu = \hat{\mu}$ is infeasible. The parameters e_margin and c_e were tuned to achieve robustness against deviations from the planned path while not overly restricting the vehicle.

Numerical values of the parameters used in the acceleration follower are given in Table 4. The gain K is set large enough to track the desired slip angles by steering. The parameter ω is tuned to obtain reasonable desired yaw moments and the parameters λ_max, S, and ε are tuned to track this yaw moment. The parameters $B^*_{y,i}$ and $C^*_{y,i}$ are the friction-limit tire model parameters used in (32). The parameters τ_i are tuned to limit chattering from replanning and are set to the same

Table 3. Parameters of the motion planner

Notation	Value
$\hat{\mu}$	1.07
k	1.25
K_d	$1.71 \times 10^{-4}\,\mathrm{m}^{-1}$
$s_f - s_s$	30 m
e_{margin}	0.5 m
v^2_{min}	$1\,\mathrm{m}^2/\mathrm{s}^2$
σ_{min}	$-\pi/2 + 0.1$ rad
σ_{max}	$\pi/2 - 0.1$ rad
c_e	1×10^4
c_μ	1×10^{10}
N	50

Table 4. Parameters of the acceleration follower

Notation	Value
K	19
ω	5
λ_{max}	2
S	0.05
ε	$1/I_{zz}$
$B^*_{y,1}$, $B^*_{y,2}$	3.2931
$C^*_{y,1}$, $C^*_{y,2}$	2.2497
$B^*_{y,r}$	3.9338
$C^*_{y,r}$	1.9536
τ_r	0.2
τ_1, τ_2	0.01
γ_T	0.85

order or smaller as the time response of the yaw or steering dynamics. Finally, γ_T is tuned to prevent wheel lock because of braking.

7.1 Straight-Road Scenario

In the first scenario, a straight road is considered, and the obstacle is static ($v_{\mathrm{obs}} = 0\,\mathrm{km/h}$ in (39)). Figure 4 shows the evolution of the maneuver as the vehicle moves along the road. The vehicle is at $X = 0$ and $Y = 0$ when the obstacle is detected. For the first two meters, a standard strategy of straight-line braking is used. When at 18 m away from the obstacle, the first plan computed is ready and the vehicle starts to follow it. As the obstacle avoidance continues, the plan is updated to account for possible disturbances and differences in dynamics between the model used in the motion planner and the vehicle.

Further into the maneuver, it can be observed in Fig. 5 that the initially planned velocity reduction starts to significantly differ at around 23 m, as the motion planner demands more lateral acceleration $a_\perp$ at the cost of longitudinal acceleration a_v to ensure that the vehicle does not hit the road border. At this point, the most significant threat of the obstacle has already been passed. Figure 5 also shows the acceleration reference θ^s used in the acceleration follower, where the reference $\theta^s = 180°$ corresponds to braking along the path, with a

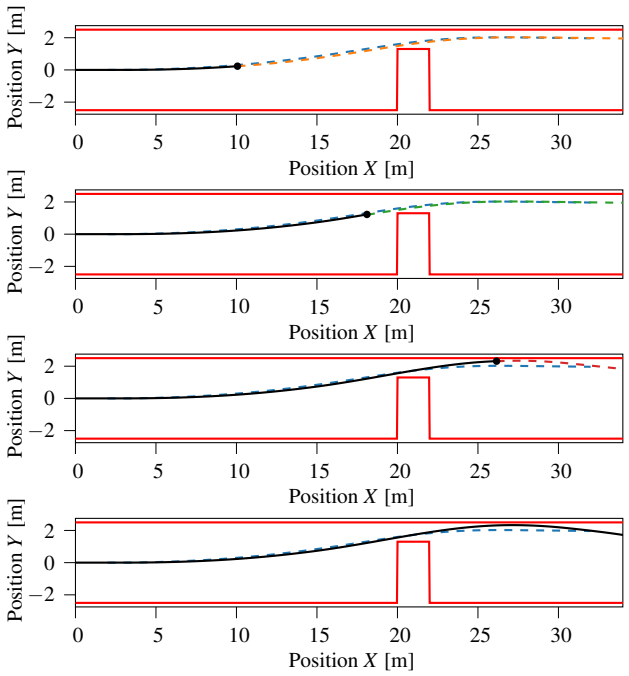

Fig. 4. Evolution of the maneuver for the straight-road scenario. The small black dot is the current position of the car with a black line showing its path. The blue dashed line is the first planned path. The remaining dashed line is the latest planned path. The red lines mark the position constraints.

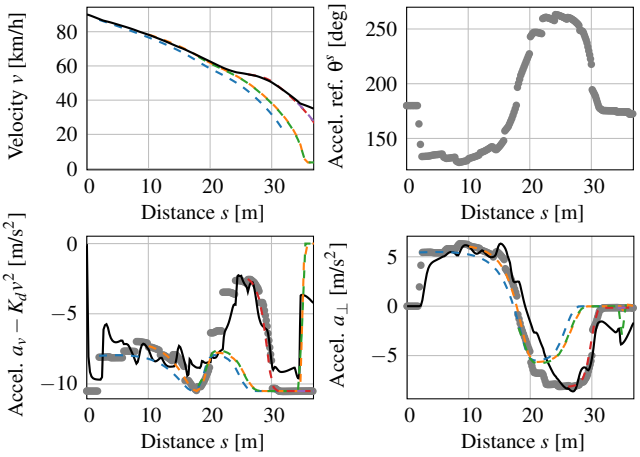

Fig. 5. Velocity and acceleration for the straight-road scenario. The black lines are the resulting values. In the velocity and acceleration plots, every fourth plan computed is shown as dashed. In the acceleration plots, the reference values are shown in gray.

lower value corresponding to an acceleration towards the left and a larger value corresponding to an acceleration towards the right.

Variables related to body slip are plotted in Fig. 6. It can be observed that the body slip is kept within modest values. The approximation of the yaw moment using the friction-ellipse based tire model (25) gives a reasonable approximation of the true yaw moment, and the update of λ (24) tracks this

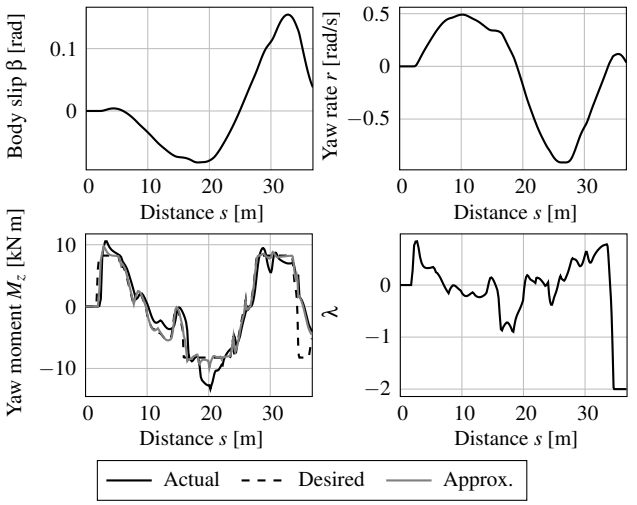

Fig. 6. Body-slip related variables for the straight-road scenario. The black lines are the resulting values. In the yaw moment plot, the dashed line is the desired value and the gray line is the approximated value.

yaw moment well. Towards the end of the maneuver, the value of λ is saturated because of the time required to achieve the desired yaw moment; at this point the vehicle is traveling at around 40 km/h.

In Fig. 7, the steering angle is shown together with the slip angles of the front wheels, the lumped rear slip angle, and the braking torques. The desired front slip angles are seen to be tracked well, where it should be noted that only one of the slip angles is tracked at a time because of the common steering angle. Some lag is seen in the tracking of the rear slip angle because of the significantly slower yaw dynamics and the time constant τ_r of the first-order filter (34d). The braking torques of the front wheels are significantly heavier than those for the rear wheels because of the load transfer resulting from heavy braking. With the exception of the part right after passing the obstacle at around 22 m to 30 m, the braking effort can be seen to be large throughout the maneuver.

7.2 Curved-Road Scenarios

In the curved-road scenarios, the road starts straight and then turns left or right with a curvature of $\pm 0.01\,\mathrm{m}^{-1}$ after 10 m, i.e.,

$$\kappa(s) = \begin{cases} 0, & \text{if } s < 10, \\ \pm 0.01, & \text{if } s \geq 10. \end{cases} \tag{66}$$

These scenarios give insight into how the vehicle accounts for the road curvature when achieving safe avoidance. Figure 8 shows the paths for both scenarios, while Fig. 9 and Fig. 10 show the resulting velocity and acceleration reference for each scenario. In the case of the left-hand turn, the obstacle becomes harder to avoid but it becomes easier to avoid the lane border after passing the obstacle. In the case of the right-hand turn, the opposite is true. This can be seen in

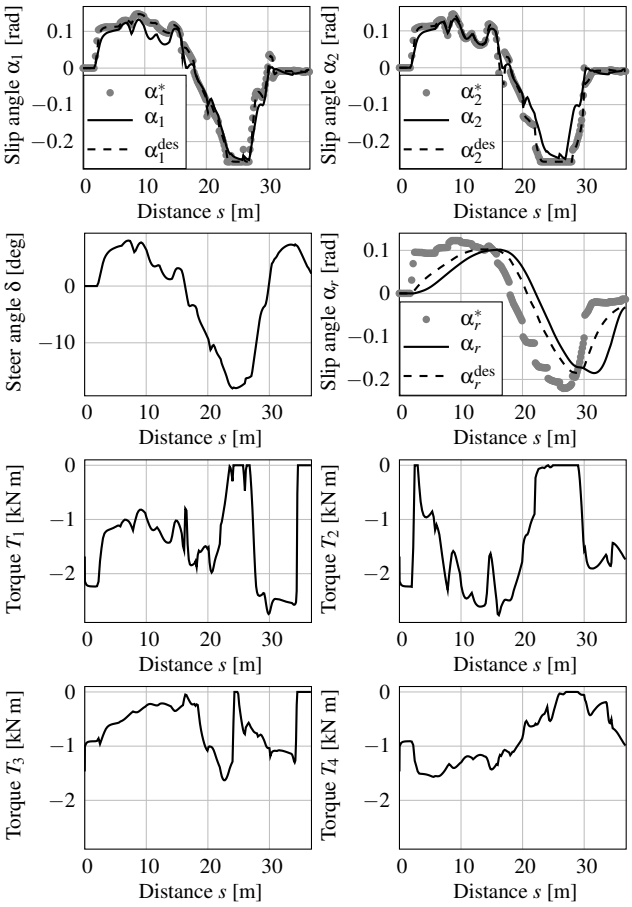

Fig. 7. Steering angle, slip angles, and braking torques for the straight-road scenario. The black lines are the resulting angles. In the slip-angle plots, the reference values are shown in gray, with the filtered references shown as dashed.

Fig. 9 and Fig. 10, where the acceleration reference θ^s in the left-hand turn specifies more heavy braking (closer to $\theta^s = 180°$) after passing the obstacle, while during the right-hand turn it specifies more heavy braking before reaching the obstacle. Further, the vehicle reduces the vehicle speed to around 61 km/h before reaching the obstacle in the right-hand turn, but only to about 70 km/h in the left-hand turn.

7.3 Moving-Obstacle Scenario

In the moving-obstacle scenario, the left-hand turn scenario is studied again, but now the obstacle moves such that the obstacle region on the road is getting smaller (as the moose walks across the road). The obstacle velocity in (39) is $v_{\text{obs}} = 1\,\mathrm{m/s}$. As the scenario progresses, the plan is updated in accordance with the new obstacle positions (see Fig. 11). Because of the moving obstacle, the vehicle is able to change to a strategy of more heavy braking, and reduce the speed to 63 km/h before reaching the obstacle, while for the stationary obstacle the speed is reduced only to 70 km/h (compare the velocity at $s = 20\,\mathrm{m}$ in Fig. 9 and Fig. 12). This is a very positive outcome of the real-time replanning and control strategy.

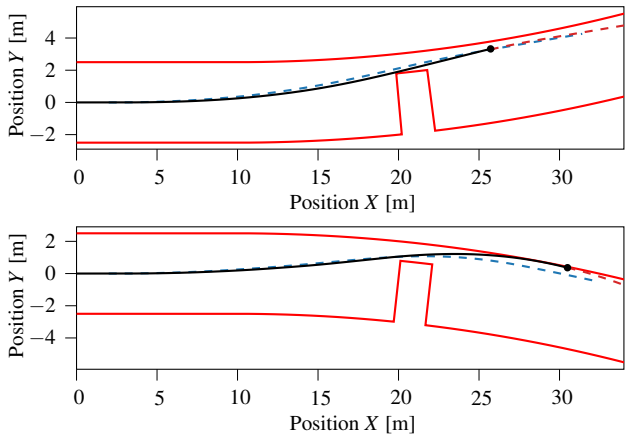

Fig. 8. Path for the left-curved road scenario (top) and the right-curved scenario (bottom). The red lines mark the position constraints. The small black dot is the current position of the car with a black line showing its path. The blue dashed line is the first planned path. The red dashed line is the latest planned path.

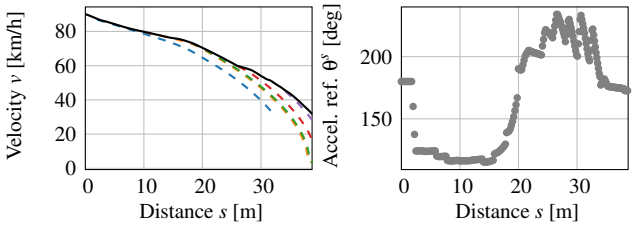

Fig. 9. Velocity and acceleration reference for the left-curved road scenario. The black line is the resulting velocity. In the velocity plot, every fourth plan computed is shown as dashed. In the acceleration plot, the reference values are shown in gray.

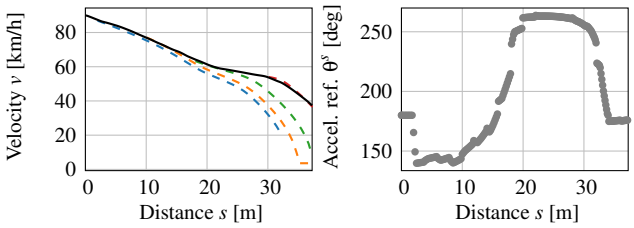

Fig. 10. Velocity and acceleration reference for the right-curved road scenario. The black line is the resulting velocity. In the velocity plot, every fourth plan computed is shown as dashed. In the acceleration plot, the reference values are shown in gray.

7.4 Real-Time Performance

The computational time spent in the motion planner is shown in Fig. 13 for each of the scenarios. For cases where the computation is not finished before reaching the starting position s_s of the plan, a gap in the line is shown. This is only the case in the challenging right-hand turn after the obstacle has been passed, specifically at 24 m, 26 m, and 34 m along the road. In these cases the last plan computed is used resulting in the successful maneuver shown in Fig. 8, which is possible because the planning horizon is 30 m. In all other cases, the plan is computed well in time, with a typical value below 50 ms. This corresponds to a plan every 2 m for a velocity up to 144 km/h, which is above most posted speed limits around the world. The computation time for the acceleration follower is negligible compared to that for the motion planner.

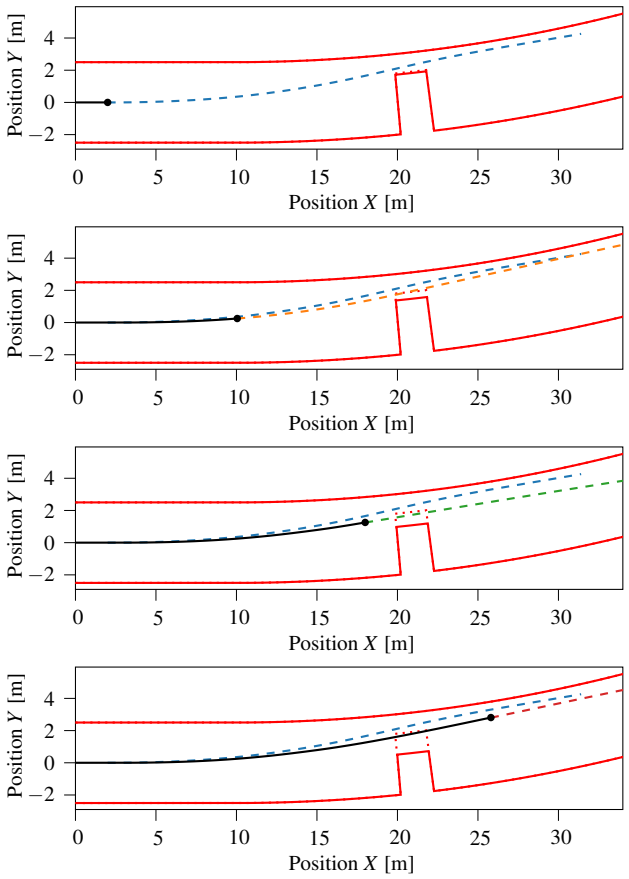

Fig. 11. Evolution of the maneuver for the moving-obstacle scenario. The red lines mark the position constraints with the dotted red line marking the obstacle constraint at the start of the maneuver. The small black dot is the current position of the car with a black line showing its path. The blue dashed line is the first planned path. The remaining dashed line is the latest planned path.

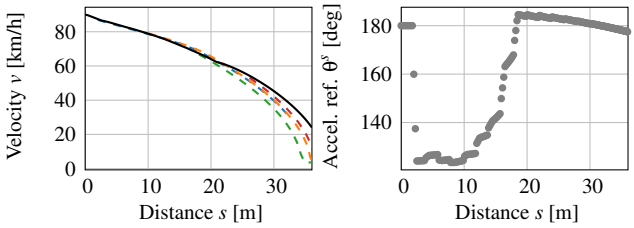

Fig. 12. Velocity and acceleration reference for the moving-obstacle scenario. The black line is the simulated velocity. In the velocity plot, every fourth plan computed is shown as dashed. In the acceleration plot, the reference values are shown in gray.

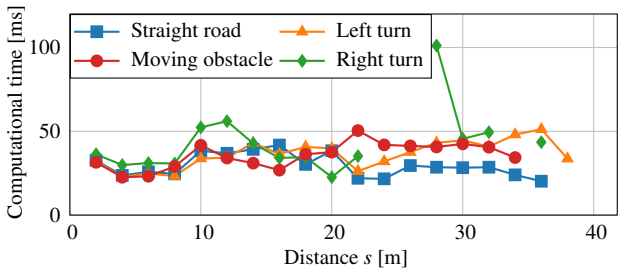

Fig. 13. Computational time spent in the motion planner as a function of the position s, where s is the starting position for which the computed plan is used as the reference. Plans not finished in time or not converged are shown as a gap in the lines, in which case the previous plan is used. Performed on a laptop with the CPU i7-8550U.

8 Discussion

The optimal control problem (9) was formulated with the safety consideration to favor heavy braking to reduce velocity as much as possible, while still being able to both avoid obstacles and stay on the road. It is thus interesting to see how this is achieved in the different scenarios: straight road, curved roads, and moving obstacle. The velocity profiles in Fig. 5, Fig. 9, Fig. 10, and Fig. 12 show that heavy braking is achieved in all cases with different velocity reduction depending on the scenario. As observed comparing Fig. 9 and Fig. 10, the curvature of the road is essential in determining the possible velocity reduction while avoiding the obstacle and staying on the road. Further, comparing Fig. 9 and Fig. 12 it is seen that the controller really utilizes the fact that the obstacle is moving and leaving more room for the vehicle. Then braking can be heavier, which is seen in the larger velocity reduction for the moving-obstacle scenario.

In addition to velocity reduction, it is desirable that the vehicle performs deftly during the maneuver. Figure 4, Fig. 8, and Fig. 11 all show that the paths are well behaved. Further, in all cases the steering angle, the slip angles, and the body slip are also well behaved, even though it is only shown for the straight-road scenario, see Fig. 6 and Fig. 7. The controller results in an excellent balance between avoidance and heavy braking. Further, in Section 7.4, it is demonstrated that the controller can run in real time, with planning updates every 2 m and with the low-level acceleration follower running at 1000 Hz.

9 Conclusions

A fundamental question for critical avoidance maneuvers is how to achieve heavy braking while still leaving room for a maneuver that both avoids the obstacle and keeps the vehicle on road. This is here captured in an optimization formulation penalizing velocity, where obstacles and road borders are represented as constraints. Considering both obstacle avoidance and road borders, an analytical solution is not available, not even for a particle model. Thus, a numerical approach is needed and the following key ideas have been used. A motion-planning step based on receding-horizon planning is used to obtain a sequence of acceleration-vector references, and then a force-vectoring approach is used to turn these references into actuator commands.

The controller is evaluated in a number of representative scenarios using a double-track vehicle model with load transfer and wheel dynamics. In all cases, the vehicle is well behaved regarding steering angles, slip angles, body slips, and the resulting paths. It is also demonstrated that the controller successfully balances braking and avoidance such that it really takes advantage of the braking possibilities. Specifically, it is shown for a moving obstacle that the controller benefits from a widening gap in terms of velocity decrease, which is a clear advantage of the online replanning capability if the obstacle is a moving human or animal. Finally, real-time capabilities have been demonstrated in that the planning step can run each 2 m and the acceleration follower can run in 1000 Hz. In conclusion, the controller performs well both from a functional perspective and from a real-time perspective.

Funding

This work was supported by the ELLIIT Strategic Area for ICT research, supported by the Swedish Government, and by the Wallenberg AI, Autonomous Systems and Software Program (WASP) funded by the Knut and Alice Wallenberg Foundation.

References

[1] Olofsson, B., and Nielsen, L., 2020. "Using crash databases to predict effectiveness of new autonomous vehicle maneuvers for lane-departure injury reduction". *IEEE Trans. Intell. Transp. Syst.* DOI 10.1109/TITS.2020.2983553.

[2] SAE International, 2018. Taxonomy and definitions for terms related to driving automation systems for on-road motor vehicles. Standard J3016_201806.

[3] Dingle, P., and Guzzella, L., 2010. "Optimal emergency maneuvers on highways for passenger vehicles with two- and four-wheel active steering". In Amer. Control Conf. (ACC), pp. 5374–5381.

[4] Gao, Y., Gordon, T., and Lidberg, M., 2019. "Optimal control of brakes and steering for autonomous collision avoidance using modified Hamiltonian algorithm". *Veh. Syst. Dyn.,* **57**(8), pp. 1224–1240.

[5] Brown, M., and Gerdes, J. C., 2020. "Coordinating tire forces to avoid obstacles using nonlinear model predictive control". *IEEE Trans. Intell. Veh.,* **5**(1), pp. 21–31.

[6] Velenis, E., and Tsiotras, P., 2005. "Minimum time vs maximum exit velocity path optimization during cornering". In Proc. IEEE Int. Symp. Ind. Electron. (ISIE), pp. 355–360.

[7] Sharp, R. S., and Peng, H., 2011. "Vehicle dynamics applications of optimal control theory". *Veh. Syst. Dyn.,* **49**(7), pp. 1073–1111.

[8] Berntorp, K., Olofsson, B., Lundahl, K., and Nielsen, L., 2014. "Models and methodology for optimal trajectory generation in safety-critical road-vehicle manoeuvres". *Veh. Syst. Dyn.,* **52**(10), pp. 1304–1332.

[9] Limebeer, D., and Rao, A., 2015. "Faster, higher, and greener: Vehicular optimal control". *IEEE Control Syst. Mag.,* **35**(2), pp. 36–56.

[10] Stigson, H., Kullgren, A., and Rosén, E., 2012. "Injury risk functions in frontal impacts using data from crash pulse recorders". In 56th Ann. Adv. Automot. Med. (AAAM), Vol. 56, pp. 267–276.

[11] Subosits, J. K., and Gerdes, J. C., 2019. "From the racetrack to the road: Real-time trajectory replanning for autonomous driving". *IEEE Trans. Intell. Veh.,* **4**(2), pp. 309–320.

[12] Svensson, L., Bujarbaruah, M., Kapania, N. R., and Törngren, M., 2019. "Adaptive trajectory planning and optimization at limits of handling". In 2019 IEEE/RSJ Int. Conf. Intell. Robots and Syst. (IROS), pp. 3942–3948.

[13] Viana, I. B., Kanchwala, H., Ahiska, K., and Aouf, N., 2021. "A comparison of trajectory planning and control frameworks for cooperative autonomous driving". *ASME. J. Dyn. Sys., Meas., Control,* **143**(7).

[14] Kapania, N. R., and Gerdes, J. C., 2015. "Design of a feedback-feedforward steering controller for accurate path tracking and stability at the limits of handling". *Veh. Syst. Dyn.,* **53**(12), pp. 1687–1704.

[15] Yang, D., Jacobson, B., Jonasson, M., and Gordon, T. J., 2014. "Closed-loop controller for post-impact vehicle dynamics using individual wheel braking and front axle steering". *Int. J. Veh. Auton. Syst.,* **12**(2), pp. 158–179.

[16] Gao, Y., Lidberg, M., and Gordon, T. J., 2015. "Modified Hamiltonian algorithm for optimal lane change with application to collision avoidance.". *MM Science J.*, pp. 576–584.

[17] Fors, V., Olofsson, B., and Nielsen, L., 2019. "Yaw-moment control at-the-limit of friction using individual front-wheel steering and four-wheel braking". In 9th IFAC Symp. Advances Automot. Control (AAC), pp. 458–464.

[18] Gao, Y., Lin, T., Borrelli, F., Tseng, E., and Hrovat, D., 2010. "Predictive control of autonomous ground vehicles with obstacle avoidance on slippery roads". In ASME 2010 Dyn. Syst. and Control Conf. (DSCC), pp. 265–272.

[19] Shiller, Z., and Sundar, S., 1998. "Emergency lane-change maneuvers of autonomous vehicles". *ASME. J. Dyn. Sys., Meas., Control,* **120**(1), pp. 37–44.

[20] Klomp, M., Lidberg, M., and Gordon, T. J., 2014. "On optimal recovery from terminal understeer". *Proc. Inst. Mech. Eng., Part D, J. Automobile Eng.,* **228**(4), pp. 412–425.

[21] Pacejka, H., 2006. *Tyre and vehicle dynamics*, second ed. Butterworth-Heinemann, Oxford, UK.

[22] Bock, H. G., and Plitt, K. J., 1984. "A multiple shooting algorithm for direct solution of optimal control problems". In 9th IFAC World Congr., pp. 1603–1608.

[23] Andersson, J. A. E., Gillis, J., Horn, G., Rawlings, J. B., and Diehl, M., 2019. "CasADi – A software framework for nonlinear optimization and optimal control". *Math. Program. Comput.,* **11**(1), pp. 1–36.

[24] Wächter, A., and Biegler, L. T., 2006. "On the implementation of an interior-point filter line-search algorithm for large-scale nonlinear programming". *Math. Program.,* **106**(1), pp. 25–57.

[25] HSL, 2020. A collection of Fortran codes for large scale scientific computation. Accessed: 2020-10-26.

[26] Arikere, A., Yang, D., and Klomp, M., 2019. "Optimal motion control for collision avoidance at left turn across path/opposite direction intersection scenarios using electric propulsion". *Veh. Syst. Dyn.,* **57**(5), pp. 637–664.

[27] Subosits, J. K., and Gerdes, J. C., 2017. "A synthetic input approach to slip angle based steering control for autonomous vehicles". In Amer. Control Conf. (ACC), pp. 2297–2302.

[28] Wong, J. Y., 2008. *Theory of Ground Vehicles*, fourth ed. Wiley, Hoboken, NJ.